Revision 2

Raman signatures of the distortion and stability of $MgCO_3$ to 75 GPa

Chaoshuai Zhao[1], Chaojia Lv[1], Liangxu Xu[1,2], Lin Liang[1,3], Jin Liu[1,]*

[1]Center for High Pressure Science and Technology Advanced Research (HPSTAR), 100094 Beijing, China
[2]College of Materials Science and Engineering, Nanjing Tech University, 211816 Jiangsu, China
[3]School of Earth and Space Sciences, Peking University, 100871 Beijing, China

*Correspondence to: J. Liu (jin.liu@hpstar.ac.cn)

Abstract

Knowledge of the stability of carbonate minerals at high pressure is essential to better understand carbon cycle deep inside the Earth. The evolution of Raman modes of carbonates with increasing pressure can straightforwardly illustrate lattice softening and stiffening. Here, we reported Raman modes of natural magnesite $MgCO_3$ up to 75 GPa at room temperature using helium as a pressure-transmitting medium (PTM). Our Raman spectra of $MgCO_3$ showed the splitting of T and v_4 modes initiates at approximate 30 and 50 GPa, respectively, which could be associated with its lattice distortions The $MgCO_3$ structure was referred to as $MgCO_3$-Ib at 30–50 GPa and as $MgCO_3$-Ic at 50–75 GPa. Intriguingly, at 75.4 GPa some new vibrational signatures appeared around 250–350 and ~800 cm^{-1}. The emergence of those Raman bands in $MgCO_3$ under relatively hydrostatic conditions is consistent with the onset pressure of structural transition to $MgCO_3$-II reported by theoretical predictions and high pressure-temperature experiments. This study suggests that hydrostatic conditions may significantly affect the structural evolution of $MgCO_3$ with increasing pressure, which shall be considered for modeling the carbon cycle in the Earth's lower mantle.

Keywords: carbonate; high pressure; Raman spectroscopy; lattice distortion

Introduction

Carbonate minerals play a significant role in the deep-carbon cycle of the Earth's interior (Hazen et al., 2013; Hazen and Schiffries, 2013). Geochemical and petrologic evidence indicates that carbon is subducted mainly as carbonates (e.g., Plank and Manning, 2019; Sanchez-Valle et al., 2011), potentially contributing to the deep carbon storage as well as affecting the physical and chemical properties of the Earth's interior. The presence of carbonates can dramatically affect the behavior of mantle aggregates such as melting, viscosity, electrical conductivity, thermal conductivity, and elasticity (Fu et al., 2017; Gaillard et al., 2008; Yao et al., 2018). The stability of carbonate minerals at high pressure is thus crucial to constrain the deep-carbon cycle as well as the chemistry and dynamics of many geological processes (Fu et al., 2017; Isshiki et al., 2004; Liu et al., 2015; Sun et al., 2020; Yao et al., 2018).

Among all carbonate minerals subducting into the Earth's deep interior, magnesite $MgCO_3$ has been extensively investigated as one of the most prominent deep-carbon carriers. The discovery of $MgCO_3$ in deep-diamond inclusions demonstrated their existence in the deep mantle (e.g., Wang et al., 1996). A large number of experiments and theoretical calculations have concentrated on the stability of pure $MgCO_3$ under high pressures. However, its high-pressure stability is still the subject of ongoing debates due to the influence of complicating factors such as pressure, temperature, oxygen fugacity, and bulk composition relevant to the deep mantle (e.g., Boulard et al., 2011; Fiquet and Reynard, 1999; Fiquet et al., 2002; Isshiki et al., 2004; Katsura et al., 1991; Li and Stackhouse, 2020; Lobanov and Goncharov, 2020; Oganov et al., 2008; Panero and Kabbes, 2008; Pickard and Needs, 2015; Santillán et al., 2005; Skorodumova et al., 2005).

Magnesite is in the rhombohedral structure $R\bar{3}c$ (defined as "$MgCO_3$-I"). Santillán et al. (2005) observed evident changes in the vibrational modes of $MgCO_3$-I in infrared spectra at approximate 30 GPa, together with a remarkable decrease in the pressure dependence of the v_3 mode. They used KBr as a pressure-transmitting medium (PTM). However, there were no new Raman signatures observed in the similar pressure range when the methanol-ethanol 4:1 mixture (ME), argon, and KBr were used as PTMs (Gillet et al., 1993; Williams et al., 1992). In addition, no structural transition was evidenced through XRD experiments using argon or no PTM at pressures up to 83 GPa (Fiquet et al., 2002; Katsura et al., 1991). Interestingly, it was experimentally observed that rhombohedral $MgCO_3$-I transformed into orthorhombic $MgCO_3$-II at 115 GPa and 2100 K using Al_2O_3 powder as a PTM (Isshiki et al., 2004). These experimental results were later confirmed by theoretical calculations (Skorodumova et al., 2005; Panero and Kabbes, 2008), which predict that $MgCO_3$-II becomes stable at ~113 GPa and 0 K. On the contrary, some theoretical calculations suggested that $MgCO_3$-I could transform into the $MgCO_3$-II phase with different structures including $P\bar{1}$, $C2/m$ and $P2_1/c$ at 75−85 GPa and 0 K (Li and Stackhouse, 2020; Oganov et al., 2008; Pickard and Needs, 2015). Similarly, recent high-pressure and high temperature experiments have not reached yet a consensus on the crystal structure of $MgCO_3$-II using diamond anvil cells (DAC) coupled with laser-heating X-ray diffraction (XRD) (Boulard et al., 2011; Maeda et al., 2017). Therefore, there is a large discrepancy in the structural stability of $MgCO_3$ at lower mantle pressures among existing studies, demanding further dedicated investigation.

In the present work, we collected high-pressure Raman spectra of natural $MgCO_3$ sample up to 75 GPa at room temperature in a DAC with helium (He) as a PTM. Since the deep mantle is under relatively hydrostatic conditions, the use of He as a PTM allowed us to better understand the structural evolution of $MgCO_3$ at high pressure, compared to the results in previous studies under non-hydrostatic conditions (e.g., Fiquet et al., 1994; Williams et al., 1992). The two lattice distortions in $MgCO_3$ likely occurred at 30 and 50 GPa, respectively, in the helium pressure medium while Raman spectroscopic signatures were observed for the transition from $MgCO_3$-I to -II at ~75 GPa. The lattice distortions could significantly affect the chemical bonding environments in $MgCO_3$ as well as its structural stability with increasing pressure. This result sheds new light on the stability of carbonates under quasi-hydrostatic conditions, indicating that the effect of hydrostaticity shall be taken into account for modeling the deep-carbon cycle (Efthimiopoulos et al., 2018).

Experimental Methods

Starting materials

The starting material was naturally occurring magnesite single-crystal samples from Dabie Mountain, China. The chemical composition of the magnesite sample was determined to be $MgCO_3$ with trace amounts of Ca, Fe, and Mn ($<$0.1 mol% in total) using a JEOL JXA-8200 electron microprobe. For simplicity, the sample was referred to as $MgCO_3$ thereinafter. $MgCO_3$ has the same crystal structure as calcite $CaCO_3$ on the surface of the Earth. Single-crystal X-ray diffraction analyses confirmed the $R\bar{3}c$ structure of the $MgCO_3$ sample, with lattice parameters *a* = 4.6435(17) Å and *c* =15.0361(56) Å under ambient conditions. These lattice parameters are in good agreement with previous studies (Farsang et al., 2018; Fiquet et al., 1994; Liang et al., 2017).

High-pressure Raman spectroscopy

High-pressure Raman spectra of $MgCO_3$ were collected from 120 to 1292 cm^{-1} using a Renishaw RM1000 Raman microscope equipped with a 250 mm spectrometer focal length at the Center for High Pressure Science and Technology Advanced Research (HPSTAR). The Raman signal was excited using the 532 nm wavelength of an Ar^+ laser, delivering a maximum power of 20 mW focused onto an approximately 2 μm spot by a Nikon L Plan EPI 20X, 0.35 objective. The spectral resolution was about 2 cm^{-1} with a holographic diffraction grating of 1800 lines/mm. A symmetric diamond anvil cell (DAC) was mounted with a pair of diamond anvils with 200 μm flat culets. The sample chamber was drilled in the center of a pre-indented tungsten gasket with diameter of 120 μm and thickness of ~30 μm. A platelet of single-crystal $MgCO_3$ sample with a thickness of 6–8 μm and ~30 μm in diameter was loaded into the sample chamber with the (101) crystal plane facing the incident laser beam, together with two ruby spheres as the pressure calibration. The PTM, He, was loaded into the sample chamber in the high-pressure gas loading system at HPSTAR. The use of He still maintains the hydrostatic conditions at 50 GPa (Klotz et al., 2009) and thus can avoid the influence of deviatoric stress. The pressure was determined by multiple measurements of the ruby fluorescence before and after each experimental run (Mao et al., 1986). Raman spectra fitting was carried out using the software PeakFit v4.12 with the Voigt area method.

Results and Discussion

Raman spectra of magnesite $MgCO_3$ were collected up to 75 GPa at room temperature using helium as a PTM (Figure 1). Rhombohedral carbonates (e.g., calcite, magnesite, siderite, and rhodochrosite) with the space group $R\bar{3}c$ have two lattice modes (*T* and *L* modes) and four internal modes (in-plane bend internal (v_4), symmetric stretch internal (v_1), the anti-symmetric stretch (v_3) and out-of-plane bend ($2v_2$) modes) (Boulard et al., 2012; Rividi et al., 2010). Therein, two Raman-active modes v_3 and $2v_2$ are hardly detected at high pressure due to their relatively weak intensity through diamond anvils. Four representative Raman modes at 213, 330, 737, 1095 cm^{-1} corresponding to T, L, v_4, and v_1, respectively, were collected for $MgCO_3$ at ambient conditions. These Raman mode values agree with previously reported literature values (Boulard et al., 2012; Farsang et al., 2018; Liang et al., 2018; Rividi et al., 2010). The T and L lattice modes result from the interactions between Mg^{2+} and CO_3^{2-} ions, while the v_4 and v_1 modes from the in-plane bending and symmetric stretching of the CO_3^{2-} units, respectively (Farsang et al., 2018).

Lattice distortion of $MgCO_3$ at high pressure

Representative high-pressure Raman spectra of $MgCO_3$ are presented in Figure 1. The splitting of T mode at 307 cm^{-1} was detected at 29.6 GPa and was observed up to at least 75 GPa the maximum pressure reached in this study. However, it is noted that Williams et al. (1992) did not observe any new Raman bands in magnesite around 30 GPa using the same method, possibly due to the broadening of Raman peaks of magnesite induced by the large deviatoric stress in the sample chamber. They used methanol-ethanol 4:1 mixture (ME) and argon as PTMs, both exhibiting non-hydrostaticity above 10 GPa (Klotz et al., 2009). That is, the splitting of T mode observed in this study might be overlapped by the broadening of Raman peaks. Alternatively, in this study, the use of He as a PTM would improve the hydrostatic conditions inside the sample chamber. The use of a soft PTM may crucially contribute to the splitting of T mode at ~30 GPa. Furthermore, another Raman peak splitting was observed in the v_4 mode at ~883 cm^{-1} at 51.1 GPa in this study (Figure 1). It was previously reported that the v_1 mode of dolomite split into four separate Raman peaks using Ne as a PTM at ~39 GPa, whereas only one peak was observed within the same Raman region when argon was used as a PTM (Efthimiopoulos et al., 2018).

Fiquet et al. (2002) carried out synchrotron XRD experiments on magnesite $MgCO_3$ up to 83 GPa without using any PTMs. They concluded that there was no structural phase transition in the investigated pressure range. The anomalous compression behavior of sharp decreases in the a/a_0, c/c_0, and V/V_0 ratios was reported in magnesite $MgCO_3$ at ~25 GPa, with silicone oil as a PTM by Fiquet et al. (1994). However, Ross (1997) suggested that such anomalies would be artificial and induced by deviatoric stress. Therefore, considering that the magnesite structure ($R\bar{3}c$) is structurally stable over 0–50 GPa, the splittings of T and v_4 modes at ~30 and ~50 GPa would not be caused by a crystal structure transition, but rather by local lattice distortions.

By comparison, the splitting of the low-frequency *T* mode at 175 cm^{-1} around 11 GPa was reported in dolomite $CaMg(CO_3)_2$, while there were no significant changes in the remaining Raman-active modes (Efthimiopoulos et al., 2017). They assigned the new mode as a result of the local structural distortion of dolomite and denoted it as the $CaMg(CO_3)_2$-Ib phase. Although the splitting of *T* mode in magnesite $MgCO_3$ occurs at ~20 GPa higher than that in dolomite, both would share the same nature. We thus would like to denote distorted magnesite as the $MgCO_3$-Ib phase (magnesite-Ib) between 30 and 50 GPa. With the emergence of the splitting of v_4 mode at about 50 GPa, the $MgCO_3$-Ib phase would undergo further distortion. Consequently, it would be denoted as the $MgCO_3$-Ic phase (magnesite-Ic) between 50−75 GPa based on the similar phenomena observed in dolomite and calcite at high pressures (Binck et al., 2019; Efthimiopoulos et al., 2017; Pippinger et al., 2015).

Both laser Raman and infrared spectroscopy can probe the local structure of neighboring atoms and groups of atoms, and they are therefore sensitive to short-range order features (Cerantola et al., 2015). Santillán et al. (2005) collected infrared spectra of magnesite up to 60 GPa with the use of KBr as a PMT. They found an unexpected negative curvature of the v_3 asymmetric-stretch mode between 30 and 50 GPa, without observing any splitting of infrared modes between 0–60 GPa. Moreover, the frequency of the v_3 mode rapidly increased above 50 GPa, likely due to the strengthening of the O-O repulsion in the CO_3^{2-} group as well as the reduction in the distance between the CO_3^{2-} groups and cations, together with a sharp decrease in the C-O band length at ~50 GPa (Fiquet et al., 2002; Santillán et al., 2005). The splitting of those modes was absent in the infrared spectroscopic measurements on $MgCO_3$. The clue may be the use of different PTMs, He versus KBr/Ar/ME, in those studies as described above in the Raman spectra of magnesite and dolomite (Efthimiopoulos et al., 2018).

The trend of intensity ratio and full width at half maximum (FWHM) provides another qualitative measure of changes in local structures. They have been successfully applied in detecting lattice distortion and phase transition of materials (e.g., siderite and water ice) using a battery of probes including Mössbauer, Raman, and X-ray absorption fine structure spectroscopy (Cerantola et al., 2015; Hirai et al., 2014; Xu et al., 1996). To further elucidate the evolution of local structures of $MgCO_3$ as a function of pressure, the intensity ratio and FWHM were analyzed here (Figures 2 and 3). The representative intensity ratios of the L/v_1 and L/v_4 of $MgCO_3$ with increasing pressure are shown in Figure 2. A clear decrease in the L/v_1 and L/v_4

ratios of $MgCO_3$ was detected from 0 to ~30 GPa. The L/v_1 values change approximately from 1.0 at ambient pressure to 0.2 at 30 GPa while the L/v_4 values change approximately from 8.4 at ambient pressure to 0.8 at 30 GPa, owing to the relatively large increase in Raman intensities of the v_1 and v_4 modes with increasing pressure. Both the intensity ratios of the L/v_1 and L/v_4 of $MgCO_3$ exhibit a plateau pattern at 0.2 and 0.7, respectively, between 30–50 GPa. A second plateau seems to appear in the L/v_1 and L/v_4 ratios approximately at 0.1 and 0.5, respectively, between 50–75 GPa. The changes in the L/v_1 and L/v_4 intensity ratios are mainly related to the change of the CO_3^{2-} group. In addition, the internal v_1 and v_4 modes rise from the symmetric and asymmetric stretching of CO_3^{2-} group and the C-O bond in CO_3^{2-} group undergoes pressure-induced shortening with increasing pressure between 0–30 GPa as proved by infrared and XRD studies (Fiquet et al., 2002; Santillán et al., 2005). With compression, the carbonate groups are pushed closer together, which changes their chemical bonds relative to the crystallographic axes and thus lead to the sharp increase of the polarizability (Chukanov and Vigasina, 2020). Hence, the pressure-induced packing of magnesite structure enhances the intensity of v_1 and v_4 modes due to the positive correlation between Raman intensity and polarizability (Larkin, 2011). On the contrary, the CO_3^{2-} group undergoes pressure-induced lengthening with increasing pressure from ~30–40 GPa (Fiquet et al., 2002; Lin et al., 2012; Santillán et al., 2005). Santillán et al. (2005) considered the C-O distance might be overestimated due to the large deviatoric stress induced by no PTM in the experiment by Fiquet et al. (2002). They suggested a minor increase in the C-O bond length from ~30–40 GPa. The process may lead to a decrease in the polarizability and thus reduce the intensity of v_1 and v_4 modes (namely, increase the L/v_1 and L/v_4 values) to some extent at 30–40 GPa. The change is more obvious in the v_1 mode because it directly relates to the C-O bond. The intensity ratios of the L/v_1 and L/v_4 further diminish as the compression of CO_3^{2-} group increases with increasing pressure. A minor deviation from the decreasing intensity trend was observed around 50 GPa possibly due to increased stiffness of the MgO_6 octahedra and CO_3 unit (C-O bond) (Fiquet et al., 2002; Santillán et al., 2005).

Furthermore, note that the FWHM values of the v_1 and v_4 modes decrease approximately from 13 to 5 cm^{-1} and from 16 to 7 cm^{-1}, respectively, at pressures up to ~15 GPa (Figure 3). The reduction in the FWHM with increasing pressure likely results from the enhancement of ordered arrangement of atoms in magnesite as observed in water and deuterated water (D_2O) at ~11 GPa

(Hirai et al., 2014; Pruzan et al., 1990; Xu et al., 1996). They found that the FWHM values of A_{1g} modes (O-H and O-D stretching mode) in ice-VII and deuterated ice-VII phase significantly decrease with increasing pressure up to ~11−13 GPa and clearly increases thereafter. The minimum of the FWHM of A_{1g} mode occurs at ~11−13 GPa, corresponding to the highest ordering of ice-VII and deuterated ice-VII (Hirai et al., 2014; Pruzan et al., 1990; Xu et al., 1996). Between 15–28 GPa, the FWHM values of the ν_1 and ν_4 modes marginally increase by ~1 cm^{-1} prior to lattice distortions occurring in magnesite. At pressure around 30 GPa, both the FWHM values of ν_1 and ν_4 modes sharply increase. Both fluctuate around 12 cm^{-1} at approximate 35−75 GPa (Figure 3). It can be attributed to the enhanced positional disorder of magnesite (Bischoff et al., 1985), resulting from the rotation of MgO_6 octahedra around the *c* axis and the associated change in C-O bond as proposed in Fiquet et al. (2002) and Santillán et al. (2005).

The structural transition of $MgCO_3$ at 75 GPa and room temperature

Interestingly, several new Raman bands appeared in the frequency range of 250–350 and ~800 cm^{-1} in $MgCO_3$ at 75 GPa and room temperature in the He pressure medium (Figure 1). Note that the XRD pattern of $MgCO_3$ was not collected due to the failure of the diamond anvils at 75 GPa. Recently, Li and Stackhouse (2020) theoretically predicted the phase transition pressure from magnesite-I to magnesite-II (space group: $P\bar{1}$) at 75 GPa and 0 K, which coincide with the same pressure as the emergence of the new Raman bands in $MgCO_3$ in the He pressure medium in this study. Meanwhile, Pickard and Needs (2015) also reported a comparable transition pressure from $R\bar{3}c$ to $P\bar{1}$ at 85 GPa from magnesite-I to magnesite-II via theoretical calculations. Hence, the $R\bar{3}c$ to $P\bar{1}$ phase transition may be responsible for new Raman bands in the frequency range between 250–350 and ~800 cm^{-1} in $MgCO_3$ at 75 GPa. Alternatively, other possible structures (i.e., C2/m, orthorhombic, etc.) could be responsible for those new vibrational modes due to the large uncertainty of phase transition pressure from theoretical calculations (Li and Stackhouse, 2020; Oganov et al., 2013; Pickard and Needs, 2015). Further high-pressure XRD experiments under hydrostatic environment are required to investigate the onset pressure of phase transition and high-pressure crystal structure of magnesite-II.

Vibrational properties of $MgCO_3$ at high pressure

Raman shifts of $MgCO_3$ with increasing pressure can be linearly fitted at 0–29, 30–50, and 50–75 GPa, respectively (Figure 4 and Table 1). At the pressure range from 0 to 29 GPa, the pressure-induced Raman shifts of T, L, v_4, and v_1 modes are 2.91, 4.20, 1.82, and 2.78 cm^{-1}/GPa, respectively. The slopes of the external modes (T and L) are generally larger than the internal modes (v_4 and v_1) due to the greater compressibility between Mg^{2+} cation and CO_3^{2-} ions than the CO_3 unit (C-O bond) (Farsang et al., 2018). Our results using He as PTM agree well with using He as PTM agree well with Liang et al. (2018) using neon (Ne). It indicates that the enhanced hydrostaticity from Ne to He has very little influence on its pressure-induced Raman shift. The dv_i/dP slopes from other studies (see Table 1) mostly range within 20% difference from our result (Farsang et al., 2018; Gillet et al., 1993; Williams et al., 1992). The deviation could be mainly attributed to the dramatic increase of shear stress above 10 GPa for the use of ME and argon as PTMs by Williams et al. (1992) and that of KBr by Gillet et al. (1993), respectively. The little discrepancy could be mainly accounted for the less pressure range using ME as PTM and composition effect of minor iron-bearing magnesite ($Mg_{0.96}Ca_{0.01}Fe_{0.03}CO_3$) from Farsang et al. (2018). At the pressure range from 30 to 50 GPa, the corresponding pressure-induced Raman shifts of T, L, v_4, and v_1 modes are 2.09, 3.12, 1.42, and 1.99 cm^{-1}/GPa, respectively. Those values further reduce to 1.77, 2.27, 1.26, and 1.86 cm^{-1}/GPa between 50 and 75 GPa (Table 2). Compared with the $MgCO_3$-I phase, the dv/dP values drop significantly by 22–28% for $MgCO_3$-Ib and 7–27% for $MgCO_3$-Ic, respectively. These results indicate that $MgCO_3$-Ib and $MgCO_3$-Ic have vibrational properties distinct from $MgCO_3$-I, and magnesite becomes stiffer when it undergoes lattice distortions. It is probable due to the large incompressibility of the CO_3^{2-} and MgO_6 octahedra with increasing pressure, which may contribute to their notable stability (Fiquet et al., 2002; Santillán et al., 2005). Therein, the increase of C-O bond length accompanied with a sharp decrease in the Mg-O bond length at pressure around 30 GPa may contribute to the lattice distortion from $MgCO_3$-I to $MgCO_3$-Ib. On the contrary, the decrease of C-O bond length accompanied with a slow decrease of Mg-O bond length at pressure around 50 GPa may contribute to the lattice distortion from $MgCO_3$-Ib to $MgCO_3$-Ic (Fiquet et al., 2002; Santillán et al., 2005).

Mode Grüneisen parameters provide important information about the relative contributions of each vibration to the thermochemical properties (Williams et al., 1992). Combined with XRD and Raman results from previous work and this study, the mode Grüneisen parameters (γ_i) were derived according to the equation as follows:

$$\gamma_i = -\frac{d\ln v_i}{d\ln V} = \frac{K_T}{v}\left(\frac{dv_i}{dP}\right) \qquad (1)$$

where v_0, V, P, and K_T are the frequency at ambient conditions in cm^{-1}, volume in Å^3, pressure in GPa and isothermal bulk model in GPa, respectively. The K_0 set as 115 GPa from Fiquet and Reynard (1999) with K'_0 fixed to 4 was used to derive the mode Grüneisen parameters γ_i of $MgCO_3$. Based on the equation (1), the γ_i value depends on the values of $1/v$ and dv/dP due to the fixed K_T at a giving pressure. It means that the lower frequency v and higher slope dv/dP corresponds to larger mode Grüneisen parameters γ_i. As shown in Table 1, the frequencies of internal modes (T and L) of $MgCO_3$ at ambient conditions are much lower than those of external modes (v_4 and v_1) while their slopes dv/dP are much larger than the latter. The γ_i for the internal modes (T and L) and external modes (v_4 and v_1) of $MgCO_3$ at ambient conditions are 1.57, 1.46, 0.28, and 0.29, respectively. The values of the internal modes are about five times of the external modes. In line with other carbonates, the major contribution to the thermodynamic Grüneisen parameters is from the T and L modes (Williams et al., 1992).

Our mode Grüneisen parameters agree with those values reported by Liang et al. (2018) using Ne as PTM. The reason should attribute the comparable hydrostaticity between He and Ne (Klotz et al., 2009). Moreover, the mode Grüneisen parameter γ_i of the T mode in magnesite is 2.6 by (Gillet et al., 1993), which is much higher than our result and other studies (Farsang et al., 2018; Liang et al., 2018). The reason is that Gillet et al. (1993) calculated the γ_i values by using the first item (value with 4.6 cm^{-1}/GPa) of second-order polynomial fitting to the dv/dP and neglected the second item (Table 1). We analyzed their data and used the linear fitting to obtain the slope. We found the value was 2.9 cm^{-1}/GPa for the linear fitting, it is similar to the values reported in this study and previous literature (Liang et al., 2018; Williams et al., 1992), which further proved our assumption. The mode Grüneisen parameters γ_i of the $MgCO_3$-Ib and $MgCO_3$-Ic phases further decrease compared to the $MgCO_3$-I phase. The corresponding mode Grüneisen parameters γ_i are listed in Table 2. Compared with the results of the high-pressure $MgCO_3$ Ib and Ic phases, the γ_i values drop significantly by 27–48% for $MgCO_3$-I to $MgCO_3$-Ib and 10–36% for $MgCO_3$-Ib to $MgCO_3$-Ic, respectively.

Implications

Raman-active modes provide bonding environments information about structures of high-pressure phases (Boulard et al., 2020; Vennari and Williams, 2018). In this study, we have detected a lower-frequency *T* mode at 29.6 GPa corresponding to a distance increasing between the CO_3^{2-}-groups and cations and a higher v_4 mode at 51.1 GPa corresponding to a strengthening of the O-O repulsion in the CO_3^{2-} group by Raman spectroscopy. The phenomena are assigned as $MgCO_3$-Ib and $MgCO_3$-Ic produced by the rotation of MgO_6 octahedra (Santillán et al., 2005). Interestingly, the stability of magnesite is improved through increasing the bond-length of CO_3 units with pressure at the expense of a weaker MgO_6 octahedra. The distorted environment of the chemical bond would greatly improve the stability of magnesite over a large pressure and temperature range and thus against its melting or decomposition (Boulard et al., 2020; Fiquet et al., 2002; Santillán et al., 2005). The similar lattice distortion was also reported in calcite (e.g., Calcite-IIIb) and dolomite (e.g., Dolomite-Ib, Dolomite-IIIb, Dolomite-IIIc) due to the distorted CaO_6 and/or MgO_6 octahedra (Binck et al., 2019; Efthimiopoulos et al., 2017; Merlini et al., 2014; Pippinger et al., 2015). More interestingly, the occurrence of the distortion phase Calcite-IIIb was evidenced in sediments in nature from the surface in quaternary loess deposits in Central Asia (Schaebitz et al., 2015). The $MgCO_3$-Ib and $MgCO_3$-Ic phases might be preserved in superdeep diamond inclusions.

Interestingly, five new Raman modes were observed at 75 GPa, which may be assigned as the magnesite-II phase with possible structures of $P\overline{1}$, C2/m, orthorhombic, etc. (Li and Stackhouse, 2020; Maeda et al., 2017; Oganov et al., 2008; Pickard and Needs, 2015). Both experimental and theoretical evidence indicate that magnesite-II represents a diversity of distorted structural environments, a corner-sharing CO_4 tetrahedra form C_3O_9 three-membered rings, within the carbonate groups and cation sites (Boulard et al., 2011; Li and Stackhouse, 2020; Oganov et al., 2008). Compared to the low-pressure threefold coordinated carbonates $(CO_3)^{2-}$ triangles in the $R\overline{3}c$ structure, the tetrahedrally coordinated carbonates are expected to exhibit substantially different reactivity and different chemical properties in the liquid state (Boulard et al., 2015). These crystallographic characteristics in carbonates may play an important role in deep carbon reservoirs and fluxes in the deep Earth (Boulard et al., 2020). Furthermore, isotopic fractionation intrinsically reflects chemical bonding environments among different phases and hence, the bonding strength in $MgCO_3$ changes through lattice distortion and structural transition, likely impacting on the distribution of carbon and magnesium isotopes in the deep mantle (Li et al., 2017).

Acknowledgments

We appreciate two anonymous reviewers for their constructive suggestions and comments, which helped improve the manuscript significantly. We also acknowledge D. Zhang and P. Dera for their helpful discussions. This study is funded by the National Key Research and Development Program of China (2019YFA0708502). J. Liu acknowledges support from the National Natural Science Foundation of China (NSFC Grant no. U1930401).

Figure captions

Figure 1. Representative Raman spectra of $MgCO_3$ at high pressures. The Raman modes are labeled according to Rividi et al. (2010). T = translational lattice mode; L = librational lattice mode; v_4 = in-plane bending internal mode; v_1 = symmetric stretching internal mode. The T, L, and v_4 modes were simultaneously enlarged to illustrate changes in the Raman spectra of $MgCO_3$. I, Ib, Ic, and II are magnesite, $MgCO_3$-Ib, -Ic and -II, respectively, in this study. Raman spectra of $MgCO_3$ show the splitting of T and v_4 modes (blue stars) at approximately 30 and 50 GPa, respectively. They are associated with lattice distortions and referred to as $MgCO_3$-Ib and $MgCO_3$-Ic, respectively. Several new Raman bands (red stars) appear at the frequencies of 250–350 and ~800 cm^{-1} in $MgCO_3$ at 75 GPa and 300 K. The emergence of those Raman bands in $MgCO_3$ under relatively hydrostatic conditions may be assigned as the $MgCO_3$-II phase.

Figure 2. The intensity ratio of L/v_1 and L/v_4 in $MgCO_3$ with increasing pressure. Dashed lines represent the changing trend of the intensity ratio of L/v_1 and L/v_4 in $MgCO_3$. The kinks in the intensity ratio of L/v_1 in $MgCO_3$ are observed around 30 GPa and 51 GPa, and are likely due to the lattice distortions of $MgCO_3$.

Figure 3. The FWHM of v_1 and v_4 modes as a function of pressure.

Figure 4. Raman shifts of $MgCO_3$ at high pressures. Raman shifts of each mode as a function of pressure can be well linearly fitted at 0–29 GPa, 29–50 GPa, and 50–75 GPa, respectively. Error bars within symbols are not shown for clarity.

Table 1. Vibrational parameters of $MgCO_3$-I at high pressures from this and previous studies.

	Mag100[a]		Mag96[b]		Mag100[c]		Mag100[d]		Mag[e]	
Raman	(He)		(ME)		(Ne)		(KBr)		(ME)	
modes	$d\nu_i/dP$	γ_i	$d\nu_i/dP$	γ_i	$d\nu_i/dP$	γ_i	$d\nu_i/dP$	γ_i	$d\nu_i/dP$	γ_i
T	2.91(10)	1.57(7)	3.52(3)	1.76	3.08(5)	1.49(2)	4.6(4) – 4.4(3)×10^{-3}	2.6	2.6(2)	1.4(1)
L	4.20(10)	1.46(5)	4.89(3)	1.59	4.49(5)	1.40(2)	4.5(3)	1.7	4.7(1)	1.67(4)
ν_4	1.82(2)	0.28(1)	1.52(4)	0.22	1.83(2)	0.26(1)	1.4(2)	0.23	1.5(2)	0.24(3)
ν_1	2.78(3)	0.29(1)	2.87(4)	0.28	2.87(2)	0.27(1)	2.5(3)	0.28	2.3(1)	0.24(2)

[a] Mag100: $Mg_{0.999}(MnFe)_{0.001}CO_3$, this study. The measured initial frequencies of Raman modes for $MgCO_3$-I at 0 GPa are chosen to retrieve the mode Grüneisen parameters γ_i, respectively. The bulk moduli K_0 set as 115 GPa from Fiquet and Reynard (1999) with K'_0 fixed to 4 was used to derive the mode Grüneisen parameters γ_i of $MgCO_3$.

[b] Mag96: $Mg_{0.96}Ca_{0.01}Fe_{0.03}CO_3$, Farsang et al. (2018).

[c] Mag100: $Mg_{0.999\pm0.001}CO_3$, Liang et al. (2018).

[d] Mag100: $MgCO_3$, Gillet et al. (1993).

[e] Mag: Unknown composition, Williams et al. (1992).

$d\nu_i/dP$ in the unit of cm^{-1}/GPa.

γ_i: Mode Grüneisen parameters.

ME: Methanol and ethanol (4:1).

Table 2. Vibrational parameters of $MgCO_3$-I, $MgCO_3$-Ib, and $MgCO_3$-Ic at high pressures.

	$MgCO_3$-I (0–29 GPa)			$MgCO_3$-Ib (29–50 GPa)			$MgCO_3$-Ic (50–75 GPa)		
Raman modes	ν_{0i} (cm^{-1})	$d\nu_i/dP$	γ_i	ν_{0i} (cm^{-1})	$d\nu_i/dP$	γ_i	ν_{0i} (cm^{-1})	$d\nu_i/dP$	γ_i
T	213	2.91(10)	1.57(7)	297	2.09(11)	0.81(5)	338	1.77(10)	0.60(4)
T				307	2.52(15)	0.94(6)	354	1.99(13)	0.62(8)
L	330	4.20(10)	1.46(5)	455	3.12(17)	0.79(5)	518	2.27(6)	0.50(2)
ν_4	737	1.82(2)	0.28(1)	790	1.42(10)	0.21(2)	821	1.26(5)	0.18(1)
ν_4							883	0.50(7)	0.07(1)
ν_1	1095	2.78(3)	0.29(1)	1177	1.99(13)	0.19(1)	1219	1.86(4)	0.18(1)

The measured initial frequencies ν_{0i} of Raman modes for $MgCO_3$-I, $MgCO_3$-Ib, and $MgCO_3$-Ic at 0, 29.6, and 51.1 GPa are chosen to retrieve the mode Grüneisen parameters γ_i, respectively. The bulk moduli K_0 set as 115 GPa from Fiquet and Reynard (1999) with K'_0 fixed to 4 was used to derive the mode Grüneisen parameters γ_i of $MgCO_3$.

$d\nu_i/dP$ in the unit of cm^{-1}/GPa.

γ_i: Mode Grüneisen parameters.

References

Binck, J., Chariton, S., Stekiel, M., Bayarjargal, L., Morgenroth, W., Milman, V., Dubrovinsky, L., and Winkler, B. (2019) High-pressure, high-temperature phase stability of iron-poor dolomite and the structures of dolomite-IIIc and dolomite-V. Physics of the Earth and Planetary Interiors, 299, 106403.

Bischoff, W.D., Sharma, S.K., and MacKenzie, F.T. (1985) Carbonate ion disorder in synthetic and biogenic magnesian calcites: a Raman spectral study. American Mineralogist, 70(5-6), 581-589.

Boulard, E., Gloter, A., Corgne, A., Antonangeli, D., Auzende, A.L., Perrillat, J.P., Guyot, F., and Fiquet, G. (2011) New host for carbon in the deep Earth. Proceeding of the National Academy of Sciences of the United States of America, 108(13), 5184-7.

Boulard, E., Guyot, F., and Fiquet, G. (2012) The influence on Fe content on Raman spectra and unit cell parameters of magnesite–siderite solid solutions. Physics and Chemistry of Minerals, 39(3), 239-246.

Boulard, E., Guyot, F. and Fiquet, G. (2020) High-pressure transformations and stability of ferromagnesite in the Earth's mantle. Carbon in Earth's Interior, 105-113.

Boulard, E., Pan, D., Galli, G., Liu, Z., and Mao, W.L. (2015) Tetrahedrally coordinated carbonates in Earth's lower mantle. Nature Communications, 6, 6311.

Cerantola, V., McCammon, C., Kupenko, I., Kantor, I., Marini, C., Wilke, M., Ismailova, L., Solopova, N., Chumakov, A., Pascarelli, S., and Dubrovinsky, L. (2015) High-pressure spectroscopic study of siderite ($FeCO_3$) with a focus on spin crossover. American Mineralogist, 100(11-12), 2670-2681.

Chukanov, N.V., and Vigasina, M.F. (2020) Vibrational (Infrared and Raman) Spectra of Minerals and Related Compounds. 1376 p, Springer, Switzerland.

Efthimiopoulos, I., Germer, M., Jahn, S., Harms, M., Reichmann, H.J., Speziale, S., Schade, U., Sieber, M., and Koch-Müller, M. (2018) Effects of hydrostaticity on the structural stability of carbonates at lower mantle pressures: the case study of dolomite. High Pressure Research, 1-14.

Efthimiopoulos, I., Jahn, S., Kuras, A., Schade, U., and Koch-Müller, M. (2017) Combined high-pressure and high-temperature vibrational studies of dolomite: phase diagram and evidence of a new distorted modification. Physics and Chemistry of Minerals, 44(7), 465-476.

Farsang, S., Facq, S., and Redfern, S.A. (2018) Raman modes of carbonate minerals as pressure and temperature gauges up to 6 GPa and 500 C. American Mineralogist: Journal of Earth and Planetary Materials, 103(12), 1988-1998.

Fiquet, G., and Reynard, B. (1999) Comparative compressibilities of calcite-structure carbonates; deviations from empirical relations. American Mineralogist, 84, 856-860.

Fiquet, G., Guyot, F., and Itie, J.-P. (1994) High-pressure X-ray diffraction study of carbonates $MgCO_3$, $CaMg(CO_3)_2$, and $CaCO_3$. American Mineralogist, 79(1-2), 15-23.

Fiquet, G., Guyot, F., Kunz, M., Matas, J., Andrault, D., and Hanfland, M. (2002) Structural refinements of magnesite at very high pressure. American Mineralogist, 87(8-9), 1261-1265.

Fu, S., Yang, J., and Lin, J.F. (2017) Abnormal elasticity of single-crystal magnesiosiderite across the spin transition in Earth’s lower mantle. Physical Review Letters, 118(3), 036402.

Gaillard, F., Malki, M., Iacono-Marziano, G., Pichavant, M., and Scaillet, B. (2008) Carbonatite melts and electrical conductivity in the asthenosphere. Science, 322(5906), 1363-1365.

Gillet, P., Biellmann, C., Reynard, B., and McMillan, P. (1993) Raman spectroscopic studies of carbonates Part I: High-pressure and high-temperature behaviour of calcite, magnesite, dolomite and aragonite. Physics and Chemistry of Minerals, 20(1), 1-18.

Hazen, R.M., Downs, R.T., Jones, A.P., and Kah, L. (2013) Carbon mineralogy and crystal chemistry. Reviews in Mineralogy and Geochemistry, 75(1), 7-46.

Hazen, R.M., and Schiffries, C.M. (2013) Why deep carbon? Reviews in Mineralogy and Geochemistry, 75(1), 1-6.

Hirai, H., Kadobayashi, H., Matsuoka, T., Ohishi, Y., and Yamamoto, Y. (2014) High pressure X-ray diffraction and Raman spectroscopic studies of the phase change of D_2O ice VII at approximately 11 GPa. High Pressure Research, 34(3), 289-296.

Isshiki, M., Irifune, T., Hirose, K., Ono, S., Ohishi, Y., Watanuki, T., Nishibori, E., Takata, M., and Sakata, M. (2004) Stability of magnesite and its high-pressure form in the lowermost mantle. Nature, 427(6969), 60-63.

Katsura, T., Tsuchida, Y., Ito, E., Yagi, T., Utsumi, W., and Akimoto, S.-i. (1991) Stability of magnesite under the lower mantle conditions. Proceedings of the Japan Academy. Ser. B: Physical and Biological Sciences, 67(4), 57-60.

Klotz, S., Chervin, J.C., Munsch, P., and Le Marchand, G. (2009) Hydrostatic limits of 11 pressure transmitting media. Journal of Physics D: Applied Physics, 42(7), 075413.

Larkin, P. (2011) Infrared and Raman Spectroscopy :principles and spetral interpretation. 228 p, Elsevier, Oxford.

Li, S.-G., Yang, W., Ke, S., Meng, X., Tian, H., Xu, L., He, Y., Huang, J., Wang, X.-C., Xia, Q., Sun, W., Yang, X., Ren, Z.-Y., Wei, H., Yongsheng Liu, Meng, F., and Yan, J. (2017) Deep carbon cycles constrained by a large-scale mantle Mg isotope anomaly in eastern China. National Science Review, 4, 111–120.

Li, Z., and Stackhouse, S. (2020) Iron-rich carbonates stabilized by magnetic entropy at lower mantle conditions. Earth and Planetary Science Letters, 531, 115959.

Liang, W., Li, Z., Yin, Y., Li, R., Chen, L., He, Y., Dong, H., Dai, L., and Li, H. (2018) Single crystal growth, characterization and high-pressure Raman spectroscopy of impurity-free magnesite ($MgCO_3$). Physics and Chemistry of Minerals, 45(5), 423-434.

Liang, W., Yin, Y., Wang, L., Chen, L., and Li, H. (2017) A new method of preparing anhydrous magnesium carbonate ($MgCO_3$) under high pressure and its thermal property. Journal of Alloys and Compounds, 702, 346-351.

Lin, J.-F., Liu, J., Jacobs, C., and Prakapenka, V.B. (2012) Vibrational and elastic properties of ferromagnesite across the electronic spin-pairing transition of iron. American Mineralogist, 97(4), 583-591.

Liu, J., Lin, J.F., and Prakapenka, V.B. (2015) High-pressure orthorhombic ferromagnesite as a potential deep-mantle carbon carrier. Scientific Reports, 5, 7640.

Lobanov, S. S. and Goncharov, A. F. (2020) Pressure-induced sp^2-sp^3 transitions in carbon-bearing phases. Carbon in Earth's Interior, 1-9.

Maeda, F., Ohtani, E., Kamada, S., Sakamaki, T., Hirao, N., and Ohishi, Y. (2017) Diamond formation in the deep lower mantle: a high-pressure reaction of $MgCO_3$ and SiO_2. Scientific Reports, 7, 40602.

Mao, H., Xu, J.-A., and Bell, P. (1986) Calibration of the ruby pressure gauge to 800 kbar under quasi-hydrostatic conditions. Journal of Geophysical Research: Solid Earth, 91(B5), 4673-4676.

Merlini, M., Crichton, W.A., Chantel, J., Guignard, J., and Poli, S. (2014) Evidence of interspersed co-existing $CaCO_3$-III and $CaCO_3$-IIIb structures in polycrystalline $CaCO_3$ at high pressure. Mineralogical Magazine, 78(2), 225-233.

Oganov, A.R., Hemley, R.J., Hazen, R.M., and Jones, A.P. (2013) Structure, bonding, and mineralogy of carbon at extreme conditions. Reviews in Mineralogy and Geochemistry, 75(1), 47-77.

Oganov, A.R., Ono, S., Ma, Y., Glass, C.W., and Garcia, A. (2008) Novel high-pressure structures of $MgCO_3$, $CaCO_3$ and CO_2 and their role in Earth's lower mantle. Earth and Planetary Science Letters, 273(1-2), 38-47.

Panero, W.R., and Kabbes, J.E. (2008) Mantle-wide sequestration of carbon in silicates and the structure of magnesite II. Geophysical Research Letters, 35(14).

Pickard, C.J., and Needs, R.J. (2015) Structures and stability of calcium and magnesium carbonates at mantle pressures. Physical Review B, 91(10), 104101.

Pippinger, T., Miletich, R., Merlini, M., Lotti, P., Schouwink, P., Yagi, T., Crichton, W.A., and Hanfland, M. (2015) Puzzling calcite-III dimorphism: crystallography, high-pressure behavior, and pathway of single-crystal transitions. Physics and Chemistry of Minerals, 42(1), 29-43.

Pruzan, P., Chervin, J.C., and Gauthier, M. (1990) Raman spectroscopy investigation of ice VII and deuterated ice VII to 40 GPa. Disorder in ice VII. Europhysics Letters 13(1), 81-87.

Rividi, N., van Zuilen, M., Philippot, P., Menez, B., Godard, G., and Poidatz, E. (2010) Calibration of carbonate composition using micro-Raman analysis: application to planetary surface exploration. Astrobiology, 10(3), 293-309.

Ross, N.l. (1997) The equation of state and high-pressure behavior of magnesite. American Mineralogist, 82, 682–688.

Sanchez-Valle, C., Ghosh, S., and Rosa, A.D. (2011) Sound velocities of ferromagnesian carbonates and the seismic detection of carbonates in eclogites and the mantle. Geophysical Research Letters, 38(24), L24315.

Santillán, J., Catalli, K., and Williams, Q. (2005) An infrared study of carbon-oxygen bonding in magnesite to 60 GPa. American Mineralogist, 90(10), 1669-1673.

Schaebitz, M., Wirth, R., Janssen, C., and Dresen, G. (2015) First evidence of $CaCO_3$-III and $CaCO_3$-IIIb high-pressure polymorphs of calcite: Authigenically formed in near surface sediments. American Mineralogist, 100(5-6), 1230-1235.

Skorodumova, N.V., Belonoshko, A.B., Huang, L., Ahuja, R., and Johansson, B. (2005) Stability of the $MgCO_3$ structures under lower mantle conditions. American mineralogist, 90(5-6), 1008-1011.

Sun, Y., Hier-Majumder, S., Xu, Y., and Walter, M. (2020) Stability and migration of slab-derived carbonate-rich melts above the transition zone. Earth and Planetary Science Letters, 531, 116000.

Vennari, C.E., and Williams, Q. (2018) A novel carbon bonding environment in deep mantle high-pressure dolomite. American Mineralogist, 103(1), 171-174.

Wang, A., Pasteris, J.D., Meyer, H.O.A., and Dele-Duboi, M.L. (1996) Magnesite-bearing inclusion assemblage in natural diamond. Earth and Planetary Science Letters, 141(1-4), 293-306.

Williams, Q., Collerson, B., and Knittle, E. (1992) Vibrational spectra of magnesite ($MgCO_3$) and calcite-III at high pressures. American Mineralogist, 77(11-12), 1158-1165.

Xu, J.-A., Yeh, H.-W., Yen, J., and Huang, E. (1996) Raman study of D_2O at high pressures in a cubic zirconia anvil cell. Journal of Raman Spectroscopy, 27(11), 823-827.

Yao, C., Wu, Z., Zou, F., and Sun, W. (2018) Thermodynamic and elastic properties of magnesite at mantle conditions: First-principles calculations. Geochemistry, Geophysics, Geosystems, 19(8), 2719-2731.

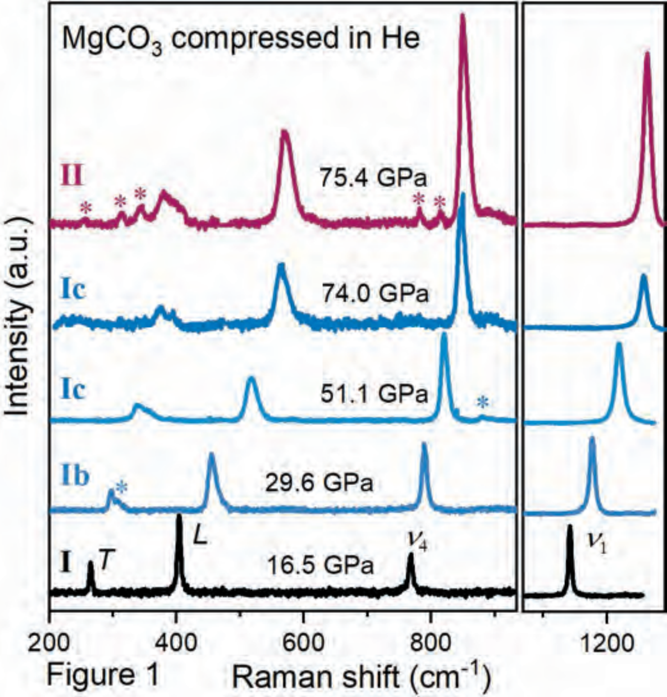
MgCO$_3$ compressed in He
II
75.4 GPa
Ic
74.0 GPa
Ic
51.1 GPa
Ib
29.6 GPa
I
T
L
ν_4
ν_1
16.5 GPa
Intensity (a.u.)
200
400
600
800
1200
Raman shift (cm^{-1})

Figure 1

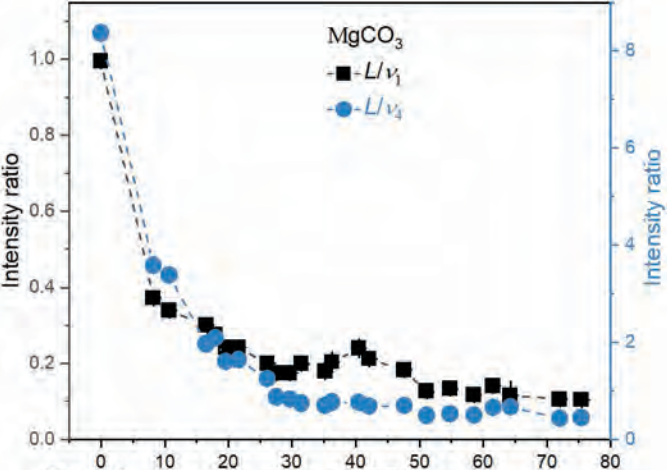

Figure 2

Pressure (GPa)

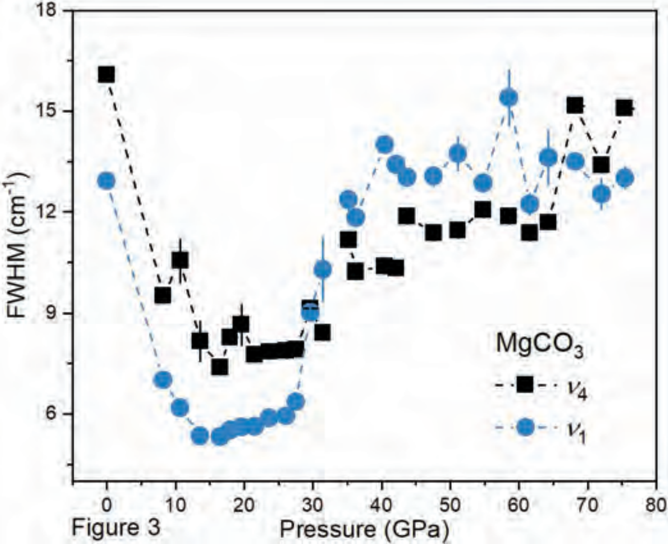
FWHM (cm^{-1})
18
15
12
9
6
0
10
20
30
40
50
60
70
80
Pressure (GPa)
MgCO$_3$
ν_4
ν_1

Figure 3

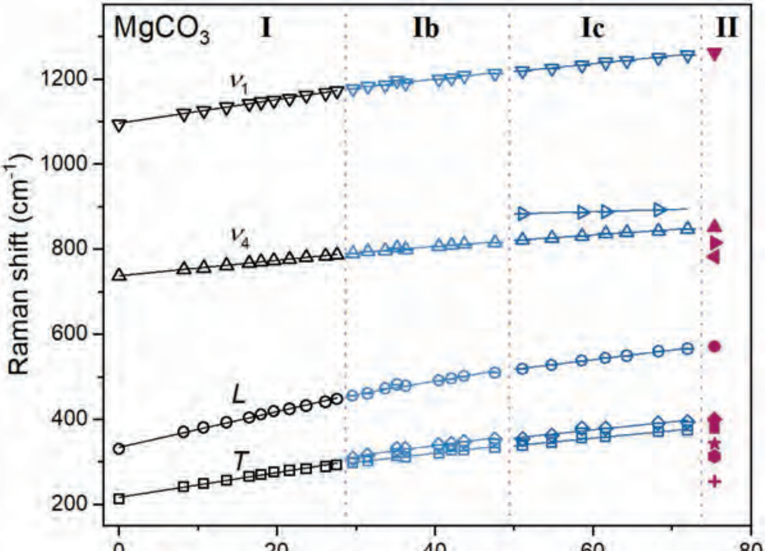
MgCO$_3$
I
Ib
Ic
II
ν_1
ν_4
L
T
Raman shift (cm^{-1})
1200
1000
800
600
400
200
0
20
40
60
80
Pressure (GPa)

Figure 4